Supplementary Information for

Dynamic and asymmetric fluctuations in the microtubule wall captured by high-resolution cryo-electron microscopy

Garrett E. Debs, Michael Cha, Xueqi Liu, Andrew R. Huehn, Charles V. Sindelar

Corresponding author: Charles V. Sindelar
Email: charles.sindelar@yale.edu

This PDF file includes:

Supplementary Information

Extended methods

Protein Purification: The same stock of protein was used for the monomeric (K349) and dimeric (K420) kinesin constructs as used in previous publications from our lab [1, 2]

Microtubule preparation: GMPCPP-stabilized microtubules were prepared using tubulin purified from bovine brain following a protocol described previously [3]. GMPCPP microtubules were polymerized by incubating 5 µM tubulin with 1 mM GMPCPP on ice for 15 minutes allowing for nucleotide exchange. The solution was then polymerized at 37°C for 3 hours before pelleting the microtubules at 40K RPM for 20 minutes. The pellet was then resuspended in EM buffer to a final concentration of ~10 µM. The EM resuspension buffer contained 25 mM Pipes at pH 6.8, 25 mM NaCl, 1 mM EGTA, and 2 mM $MgCl_2$.

Taxol-stabilized microtubules were polymerized by resuspending 250 µg of lyophilized bovine tubulin (Cytoskeleton, Denver, CO) into 25 µl of EM buffers with 2 mM GTP added. An initial pelleting step (100K RPM, 4°C, 10 minutes) was used to removed aggregated tubulin. Next, the sample was incubated for 10 minutes at 37°C before adding an equimolar concentration of Taxol. The sample was incubated for an additional 45 minutes before the microtubules were pelleted through a glycerol cushion (EM buffer with 60% glycerol). The pellet was resuspended in EM buffer to a final concentration of ~10 µM containing 20 µM Taxol.

Cryo-EM Sample Preparation: For the GMPCPP microtubule sample with monomeric kinesin, microtubules were mixed with a 2x molar excess of kinesin and incubated for 10 minutes at 24°C. 0.07 units of apyrase (Sigma, St. Louis, MO) was added and incubated for 5 minutes to hydrolyze any residual ATP. The microtubule-kinesin complex was then pelleted at 14K RPM for 15 minutes at room temperature. The sample was resuspended in EM buffer to a final concentration of 4 µM microtubules. 4 µl of sample was then added to a holey carbon grid (Quantifoil, Jena, Germany) without glow discharge. The sample was incubated on the grid for one minute before manual blotting and plunging into liquid ethane.

For the Taxol microtubule sample with sparsely decorated dimeric kinesin, microtubules were mixed with the kinesin at a 27.5% molar ratio with 2 mM ATP. The sample was incubated at room temperature for 10 minutes before the complex was pelleted at 14K RPM for 15 minutes. The pellet was then suspended in EM buffer with 0.2 µM ADP and 0.05% Nonidet P-40 (Sigma-Aldrich, Darmstadt, Germany). This sample was diluted to a final concentration of 0.275 µM microtubules and 4 µl was added to C-flat holey carbon grids (EMS, Hatfield, PA). Grids had been pre-treated using a plasma cleaner (1 second of H_2O_2). After a 1-minute incubation on the grid, the sample was blotted using a Vitrobot with a 2 second blot time and a -2 mm offset before being plunge frozen.

Data Collection: Cryo-EM micrographs were collected at 300kV on a Titan Krios (FEI, Hillsboro, OR) with K2 direct electron detectors (Gatan, Pleasanton, CA), using SerialEM for semi-automated data collection. For the GMPCPP sample, the total electron dose collected was 65 $e^-/Å^2$ distributed over 40 frames. The dataset (1,527 total micrographs) was collected at 29,000x magnification with an effective pixel size of 0.65Å using super-resolution mode. The defocus was varied between -1 and -2.5 µm. For the Taxol dataset, the total electron dose was 66 $e^-/Å^2$ distributed over 40 frames. However, only the first 15

frames were used for processing. The 5,226 micrographs collected had an effective pixel size of 0.667Å in super-resolution mode, and the defocus varied from -1.5 to -2.5 µm.

Initial Data Processing: Following data collection, the movies from both datasets were aligned using MotionCor2 [4] and 1x1 grid for motion correction. Magnification distortion correction and dose filtering were both performed during movie alignment. The resulting micrographs were then binned by two for both datasets, resulting in a pixel size of 1.3Å for the GMPCPP dataset, and 1.333Å for the Taxol dataset. CTF estimation was performed with Gctf [5] using equiphase averaging. Microtubules were then boxed using EMAN's [6] boxer and each microtubule was segmented into overlapping boxes spaced by ~80 Å.

Conventional Helical Analysis: Following boxing, microtubules were then sorted into different symmetry types. For the GMPCPP-stabilized dataset, the microtubule symmetry was determined as previously described [7]. Briefly, each microtubule segment is compared to images generated by projecting a 13 or 14-protofilament microtubule reference volume at various Euler angles. The reference projections with the highest correlation to all microtubule segments determines the microtubule symmetry type as well as the low-resolution Euler angles. In addition to determining the microtubule symmetry type, this method also determines the location of the microtubule seam for the GMPCPP-stabilized dataset due to the complete decoration of the kinesin motor domain.

For the Taxol-stabilized dataset, microtubule symmetry was determined using RELION [8] 3D Classification. Bare 12, 13, and 14-protofilament microtubules were used as reference volumes. One iteration of 3D classification was performed using 0.9-degree angular searches. Microtubules were determined to be of a specific symmetry type if at least 80% of the segments of the microtubule were classified the same. If so, the coordinates were smoothed as previously described [2]. Note the seam was not found in this case. However, to better compare the helically refined and protofilament refined maps, single seam microtubules were identified (described below) and high-resolution refinement was also performed exclusively on particles following seam identification.

Following symmetry sorting, high resolution refinement of the microtubules was performed using Helical Refinement in RELION. During refinement microtubules were treated as asymmetric tubes with a helical rise of 82 Å and a helical twist of 0°. Helical parameter searching was turned on in order to find the dimer repeat distance as well as the supertwist during refinement. After the asymmetric helical refinement, the coordinates can be symmetrized and a final helical volume was generated using the 'good' protofilament as previously described [7, 9]. Postprocessing and the final resolution of this map was calculated using RELION. Local resolution was calculated using Bsoft [10].

Protofilament Refinement: For clarity this section will be described for a 13-protofilament microtubule, even though it has been applied to each of the symmetry types in this paper. After helical analysis, the refined, asymmetric microtubule coordinates were smoothed in preparation for particle subtraction. The final asymmetric volume from RELION was used to generate subtraction volumes by using a wedge masks to remove each unique protofilament in the microtubule volume. This method resulted in 13 different volumes that would be used for subtraction. By using RELION to subtract each volume from a single microtubule segment using the smoothed, asymmetric, microtubule coordinates obtained during helical refinement, we generated stacks of protofilament particles that were 13 times the original particle stack size. The smoothed coordinates were then symmetrized so that each protofilament particle aligned to a common reference. These coordinates were then reconstructed to generate a protofilament map that would be used as the starting reference model for protofilament refinement. Additionally, this protofilament map was lowpass filtered to 20 Å and made into a mask that would be

used for refinement. The protofilament particles and their corresponding symmetrized coordinates were then treated as single particles and locally refined in RELION. For the GMPCPP dataset, the data processing ends here.

Protofilament Subtraction: Following protofilament refinement, a second round of subtraction was performed in order to minimize background signal that resulted from an initial, imperfect subtraction. Each microtubule segment was subjected to 12 rounds of subtraction using the protofilament refined coordinates and volume. The resulting protofilament particles were used for the rest of the data processing steps.

Protofilament Register Determination: After protofilament subtraction, α or β-tubulin subunits were distinguished on a per protofilament basis using RELION 3D classification. Initial efforts to sort protofilaments into the 'α/β-register' or 'β/α-register' using a random initialization gave rise to a single dominant class that lacked any distinct α or β-tubulin features. Therefore, synthetic protofilament maps were used to seed the classification. Tubulin PDBs (taken from 3J8X) [1] were fit along the length the protofilament and a synthetic volume was generated using these fit PDBs and EMAN's [6] pdb2mrc command. This volume was used as the α/β-register reference volume. The PDBs were then shifted by ~40 Å and a second synthetic volume was generated for the β/α-register reference volume. These volumes were filtered to 6 Å and used as references for RELION 3D Classification. After classification, a protofilament was determined to be in the α/β- or β/α-register if 70% of the protofilament particles classified in that register. Additionally, if not all protofilaments in the microtubule were classifiable (i.e. one protofilament had 60% classified as β/α and 40% classified as α/β) the entire microtubule was thrown out of the dataset. All β/α-register protofilaments were shifted by half a dimer repeat distance in order to put them in the α/β register. An additional round of protofilament refinement was then run. For classification of the GMPCPP-stabilized microtubules, the register of a random subset of about half of the protofilaments was shifted prior to classification. This was done in order to even out the distribution of particles into both classes. Without this step, a non-sensible "β/α-register" class would result due to lack of particles.

Following protofilament register determination, a final round of protofilament refinement was performed. The local resolution was calculated using Bsoft [10]. The same protofilament mask that was used in protofilament refinement was used during classification. All PDB fitting was done in Chimera [11].

Kinesin Classification: Following protofilament register determination, kinesin classification was performed. To maximize signal and increase the resolution, an additional round of protofilament refinement was performed prior to classification. Next, a tubulin kinesin complex PDB (3J8X) [1] was fit into the final protofilament volume and a synthetic kinesin only map was generated based off this fit using EMAN [6]. A 50 Å kinesin mask was then generated and the inverse of that mask was then applied to the final protofilament volume in order to generate a protofilament volume with a 'kinesin bite' corresponding to the kinesin binding site. This protofilament volume was subtracted from the protofilament particles leaving behind only the kinesin binding site. Classification failed to converge using default classification parameters (i.e. when all ~850K subunits were included in the classification and seeded by a random initialization), with class populations exhibiting unstable behavior over many iterations. However, we found that if the classification was restricted to a small random subset of our

data (~25K subunits), the procedure consistently converged to two classes. The resulting two classes were then used as reference to seed 3D classification of the full dataset.

PDB Refinement: To visualize an atomic model of the m-loop in the low and high rotational states, COOT was used to relax amino acids in the m-loop, in this case residues 274-287. Because our only region of interest was the m-loop during these refinements, no further structural analysis or validation was performed.

Synthetic Microtubule Processing: Two sets of synthetic micrographs were generated. The first corresponds to idealized helical symmetry of the tubulin subunits: microtubules contained 13 protofilaments, arranged so that lateral tubulin contacts follow a left-handed helix where the number of starts is 'three' if α and β tubulin are considered equivalent [12]. The second set corresponds to microtubules distorted to have non-circular cross-sections following the elastic theory of homogenous solids [13]. This resulted in series of 'squashed' microtubule cross-sections, with the angles between neighboring protofilaments deviating up to 1.4° from helical symmetry (as defined in the main text). To try and more closely represent our 'crinkled' experimental data, we use a '3-point' squashing mode, such that the microtubule cross-section will more closely resemble a triangle with rounded edges, rather than an oval. For both synthetic micrograph sets, three-dimensional positions and orientations of individual tubulin subunits were generated using an in-house MATLAB script [2], and PDB models corresponding to a tubulin-kinesin monomer complex (3J8X) [1] were mapped to these coordinates, projected, and the projections summed to generate synthetic images. The resulting synthetic micrographs were modulated by a contrast transfer function to simulate the effects of microscope defocus (200 kV accelerating voltage, 2.0 spherical aberration constant value). Microtubule in-plane orientation, rotation angle, out-of-plane tilt, and defocus values were randomized within a fixed range (in-plane and rotation angle 0-360°, out of plane +/- 15°, defocus -1 to -2.5 microns). Both sets of microtubule images used identical microtubule orientation parameters and defocus values, excepting the applied distortions.

Pre-established microtubule alignment parameters were used as a starting point for helical structure refinement, which followed the same protocol as for experimentally acquired datasets (above). For the second set of distorted-microtubule images, helical processing was followed by protofilament refinement as described above.

Distortion Analysis: Distortion was measured using the determined φ angles for each protofilament and measuring the angle between adjacent protofilaments (i.e. $\Delta\varphi_M = \varphi_n - \varphi_{n+1}$ *where n* is defined as the protofilament number in the microtubule cross-section). $\Delta\varphi_M$ was calculated for each protofilament in a microtubule segment and every segment in the microtubule. This calculation was performed for every microtubule in the dataset. For reconstructions of specific $\Delta\varphi_M$ ranges, protofilament refined coordinates corresponding to protofilament *n* were used to reconstruct the un-subtracted microtubule segment particles. PDBs could be fit into protofilaments *n* and *n+1* in the resulting microtubule maps and the angle between them were measured in Chimera [11].

Peak Separation: For data demonstrating bimodal $\Delta\varphi_M$ behavior, a double gaussian curve was fit using Python. For curve fitting, seam and non-seam $\Delta\varphi_M$ data were separated. For the 13-protofilament, GMPCPP seam data, the data was fit as is. For all other data, a bootstrap-like approach was used. The $\Delta\varphi_M$ values were resampled 1000 times and the average mean and standard deviation were used to fit the data. Following peak fitting, data for peak 1 was taken from particles two standard deviations below

the mean of peak 2. Data for peak 2 were taken from all particles two standard deviations above peak 1. For the Taxol-stabilized dataset, separated peak data corresponding to both protofilaments *n* and *n+1* were subjected to an additional round of protofilament refinement.

Autocorrelation Analysis: Autocorrelation of $\Delta\varphi_M$ was performed in Python. Autocorrelation around a microtubule cross-section was calculated using the following expressions:

$$\Delta\varphi_E = \frac{360}{N}$$

$$\Delta\varphi_D^{i,t}(n) = \Delta\varphi_M^{i,t}(n) - \Delta\varphi_E$$

$$R(a) = \frac{\sum_{t=1}^{T}\sum_{i=1}^{I_t}\sum_{n=0}^{N}\Delta\varphi_D^{i,t}(n)\Delta\varphi_D^{i,t}(n-a)}{\sum_{t=1}^{T}\sum_{i=1}^{I_t}\sum_{n=0}^{N}\Delta\varphi_D^{i,t}(n)^2}$$

Here *N* is the number of protofilaments in the microtubule and *n* is the protofilament offset. Autocorrelation values were calculated for each microtubule (*t*) in the sample (*T;* total number of microtubules), over every axial repeat (*i; I_t* total number of repeats per microtubule *t*). Here, $\Delta\varphi_D^{i,t}$ is subject to a wraparound condition, where $\Delta\varphi_D^{i,t}(-x) = \Delta\varphi_D^{i,t}(N-x)$. Due to the symmetric nature of this result, only N/2 protofilament offsets are displayed.

Autocorrelation along the length of each protofilament was calculated as:

$$R(a) = \frac{\sum_{t=1}^{T}\sum_{n=0}^{N}\sum_{i=a}^{I_t}\Delta\varphi_D^{n,t}(i)\Delta\varphi_D^{n,t}(i-a)}{\sum_{t=1}^{T}\sum_{n=0}^{N}\sum_{i=a}^{I_t}\Delta\varphi_D^{n,t}(i)^2}$$

Here, the right-most sum is restricted within the range $i = a$ to $i = I_t$ due to the lack of wraparound symmetry when $\Delta\varphi_D^{n,t}$ is considered as a function of longitudinal position along a protofilament. For this calculation, microtubules with a minimum length of 34 segments (I_t=34) were selected.

Model Building and Refinement: Tubulin structures were modeled starting with coordinates from PDB entry 3J8X [1], with Taxol taken from tubulin portion of the PDB entry 3J8X [1]. Subsequent refinements were performed using local, interactive molecular dynamics flexible fitting with Isolde [14] within the ChimeraX molecular modeling package [15]. All figures were generated with UCSF Chimera [11].

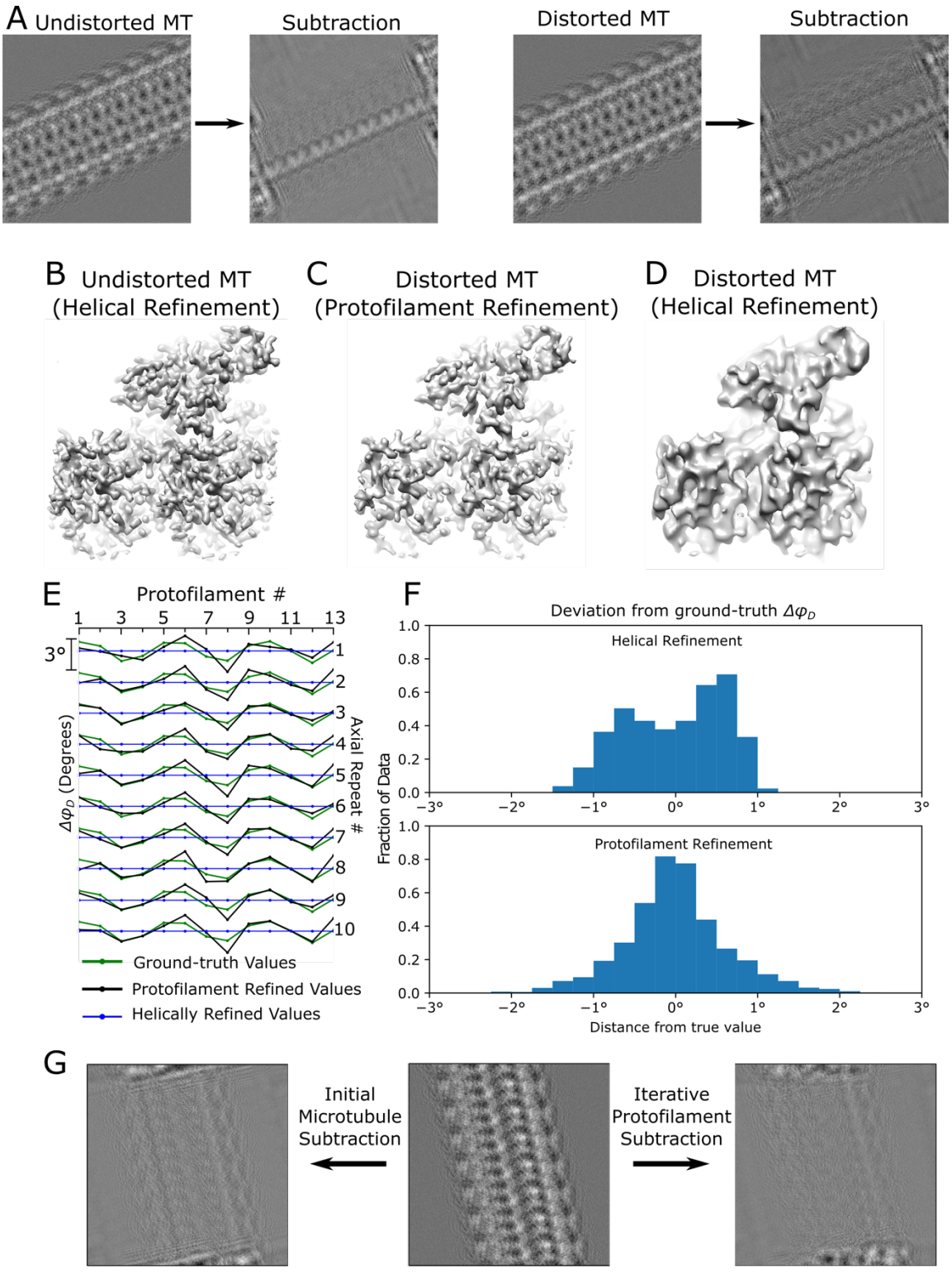

Figure S1. Protofilament refinement of synthetic microtubule images. (*A*) Subtraction of a helically symmetric microtubule model with missing protofilament from synthetically generated images of an undistorted microtubule (left two panels) and a distorted one (right two panels). Note the increase in residual background signal for the distorted case (second vs. fourth panels), which arises due to

imperfect alignment between protofilaments in the symmetric reference model and the distorted microtubule model. See panel G below. (*B*) Representative tubulin dimer with bound kinesin from the reconstruction of undistorted, synthetic microtubule particles following helical refinement. (*C, D*) Representative tubulin dimer with bound kinesin from the reconstruction of distorted, synthetic microtubule particles following protofilament refinement (*C*), and helical refinement (*D*). (*E*) Comparison of wall angle distortion angles ($\Delta\varphi_D$) for the 'ground-truth' model (values used to generate synthetic images; green) with values estimated by protofilament refinement (black) for a representative microtubule in the distorted, synthetic dataset. Note that the corresponding $\Delta\varphi_D$ estimate in a helical refinement analysis (blue) is uniformly zero (due to the assumption of symmetry). (*F*) Histogram of the errors in estimated wall angle distortion (difference of ground-truth and estimated $\Delta\varphi_D$ values) for helical refinements (top) and protofilament refinements (bottom). In contrast to the bimodal error distribution that arises from the assumption of helical symmetry (top), where zero error corresponds to a minimum in the distribution, the distribution of protofilament-refined $\Delta\varphi_D$ error values is unimodal with a maximum very close to zero. (*G*) Improved protofilament subtraction results with a synthetically modeled, distorted microtubule image following iterative subtraction with updated protofilament alignment parameters. A comparison is shown of the original, projected model image of a distorted microtubule (middle) with initial, subtracted protofilament images (left), and with the results of iterative subtraction (right). Protofilament refinement yields improved ('asymmetric') protofilament alignments, which in turn allows a follow-up subtraction to be performed yielding reduced background signal. See Extended Methods.

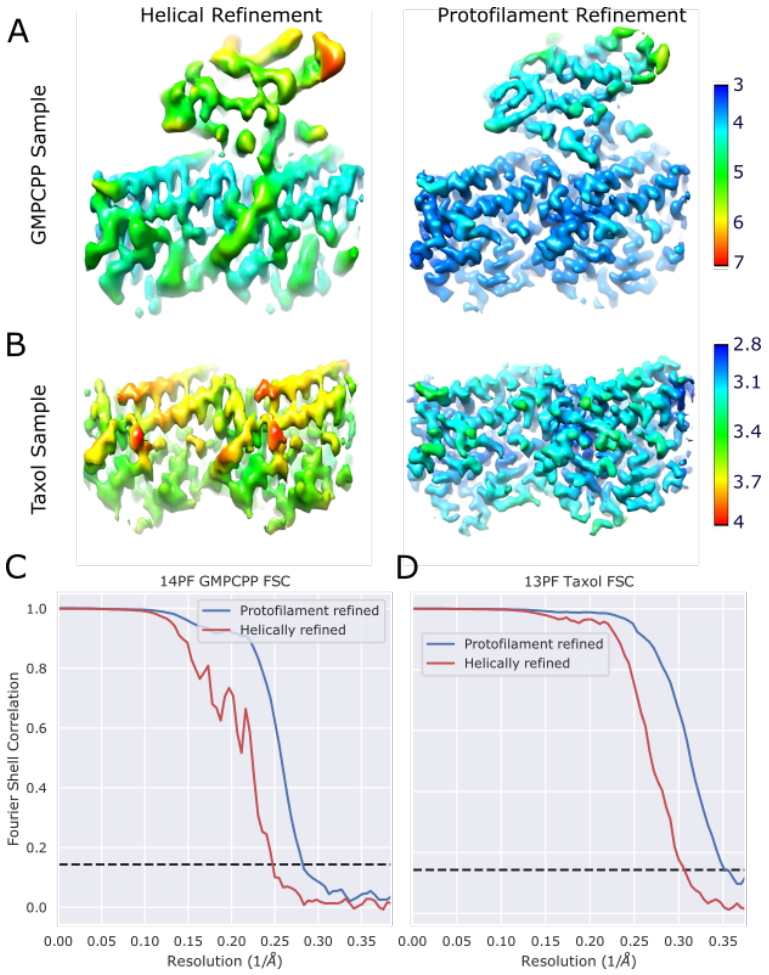

Figure S2. Improved resolution of microtubule reconstructions following protofilament refinement. (*A*) Local resolution of a 14-protofilament, GMPCPP-stabilized microtubule, fully decorated with kinesin. The left represents the reconstruction following conventional microtubule refinement methods and the right is the structure following protofilament refinement. (*B*) Local resolution of a 13-protofilament, Taxol-stabilized microtubule sparsely decorated with kinesin. Due to low kinesin occupancy, the overall refinement does not have a visible kinesin signal at this threshold (see Figure 3)**.** The local resolution was calculated using BSoft using a 0.5 FSC cutoff. Note the difference in scale bars between A and B. (*C, D*) Fourier shell correlation (FSC) resolution estimates for helical and protofilament refinements from the 14PF GMPCPP and 13PF Taxol data sets. See also Table S1.

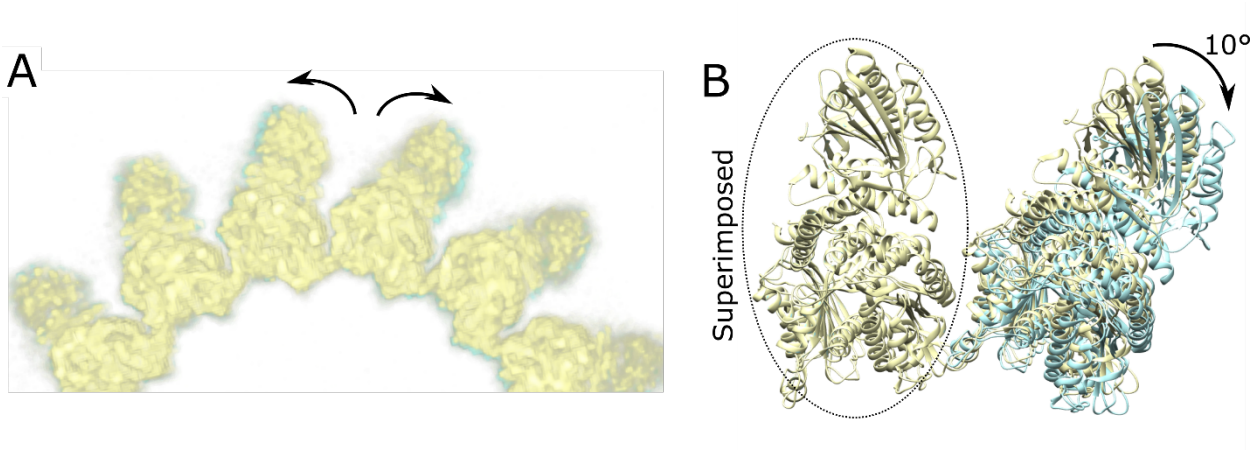

Figure S3. Validation of distorted wall geometry 3D reconstruction in Figure 4D using 'clean' helically refined alignment parameters.

A possible weakness of 3D reconstructions of distorted wall segments such as the one shown in Figure 4D is its reliance on alignments generated from the protofilament refinement procedure itself. Hence, it is conceivable, for example, that the background subtraction step during protofilament refinement gives rise to over-fitting artifacts that pathologically affect the protofilament refinement and compromise the resulting 3D structure. To address this possibility, new 3D reconstructions of the same deformed microtubule wall segments shown in Fig. 4D were generated, using a 'clean' set of alignment parameters never touched by protofilament refinement. Identified wall segments from Fig. 4D were reconstructed using substituted alignment parameters from the original, conventional microtubule refinement that was performed under the assumption of helical symmetry.

(*A*) Reconstruction of 14-protofilament GMPCPP stabilized microtubules using helically refined coordinates, corresponding to protofilament pairs with $\Delta\varphi_M \approx 21°$ (yellow) and $\Delta\varphi_M \approx 31°$ (cyan) as measured using protofilament refined alignment parameters (see Figure 4D). Overlay of the resulting structures recapitulate the geometry differences observed in the original Figure 4D- despite the new structures being mostly independent of the protofilament refinement (the only remaining connection to protofilament refinement here is its use to flag segments having a specific wall geometry). This additional control, which was repeated for the described 3D reconstructions of distorted protofilament pairs (Fig. 4F, Fig. 5E), provides additional evidence that the protofilament refinement method reliably identifies distorted microtubule wall segments.

(*B*) PDB models (3J8X) were fit into the aligned reconstructions, quantifying the relative rotation value (10°), in agreement with observation in Figure 4D made using the protofilament-refined alignment parameters.

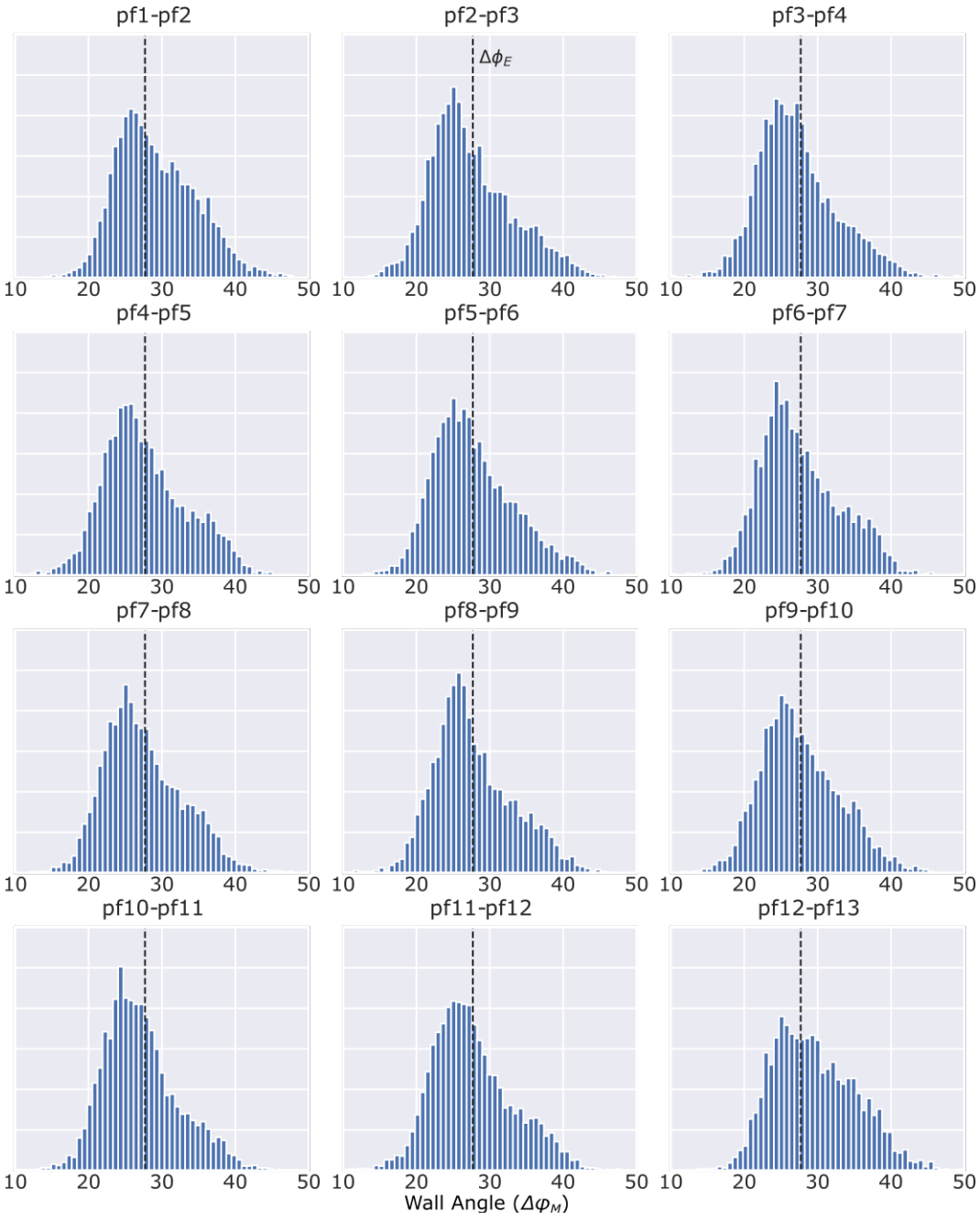

Figure S4. **Wall angle distributions for individual protofilament pairs corresponding to the low curvature geometry of the seam** (leftmost peak in the 13-protofilament GMPCPP seam angle distribution; Figure 4E, bottom). The dashed line represents the helically symmetric wall angle ($\Delta\varphi_E$).

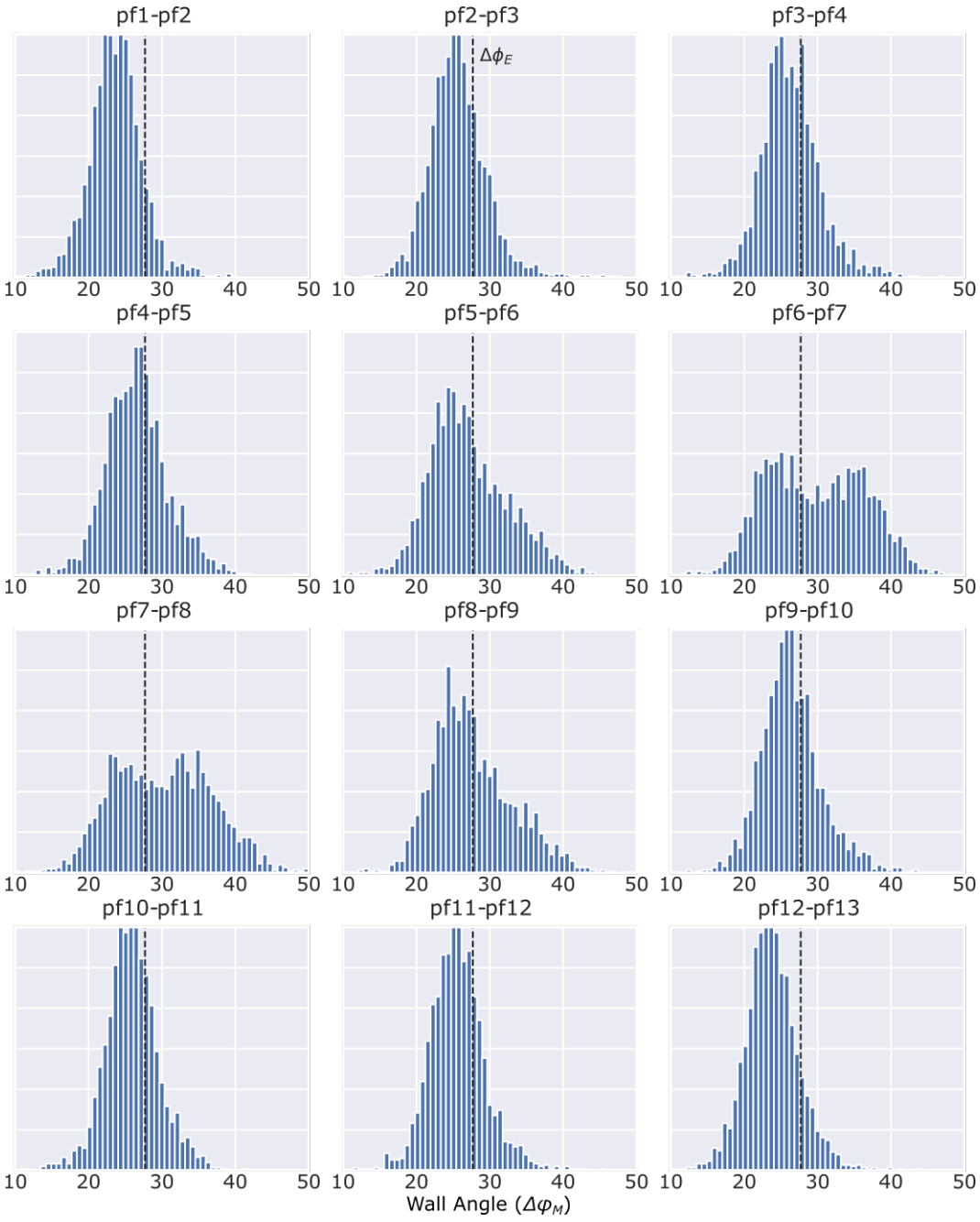

Figure S5. **Wall angle distributions for individual protofilament pairs corresponding to the 'squashed', rightmost peak in the 13-protofilament GMPCPP microtubule population** (Figure 4E bottom). The dashed line represents the helically symmetric wall angle ($\Delta\varphi_E$). The majority of the protofilament pairs prefer the low curvature state, except opposite the seam where the high curvature population is increased. This result describes a 'squashed' microtubule shape (Figure 6F).

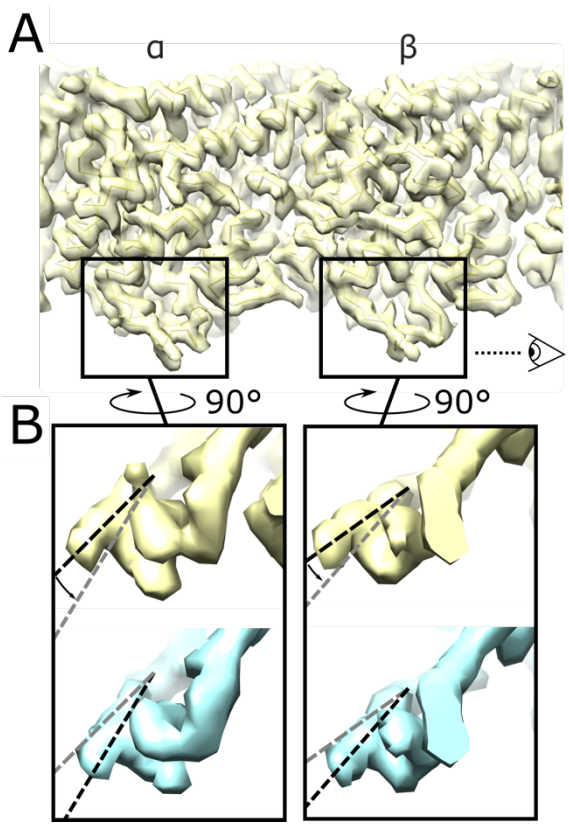

Figure S6. Structural differences between the low and high curvature m-loop conformations. (A) 3D reconstruction corresponding to particles in the low curvature state as defined in Figure 5A. (B) Close up view of the m-loops in (A) (top) and for the equivalent 3D reconstruction of the high curvature state (bottom).

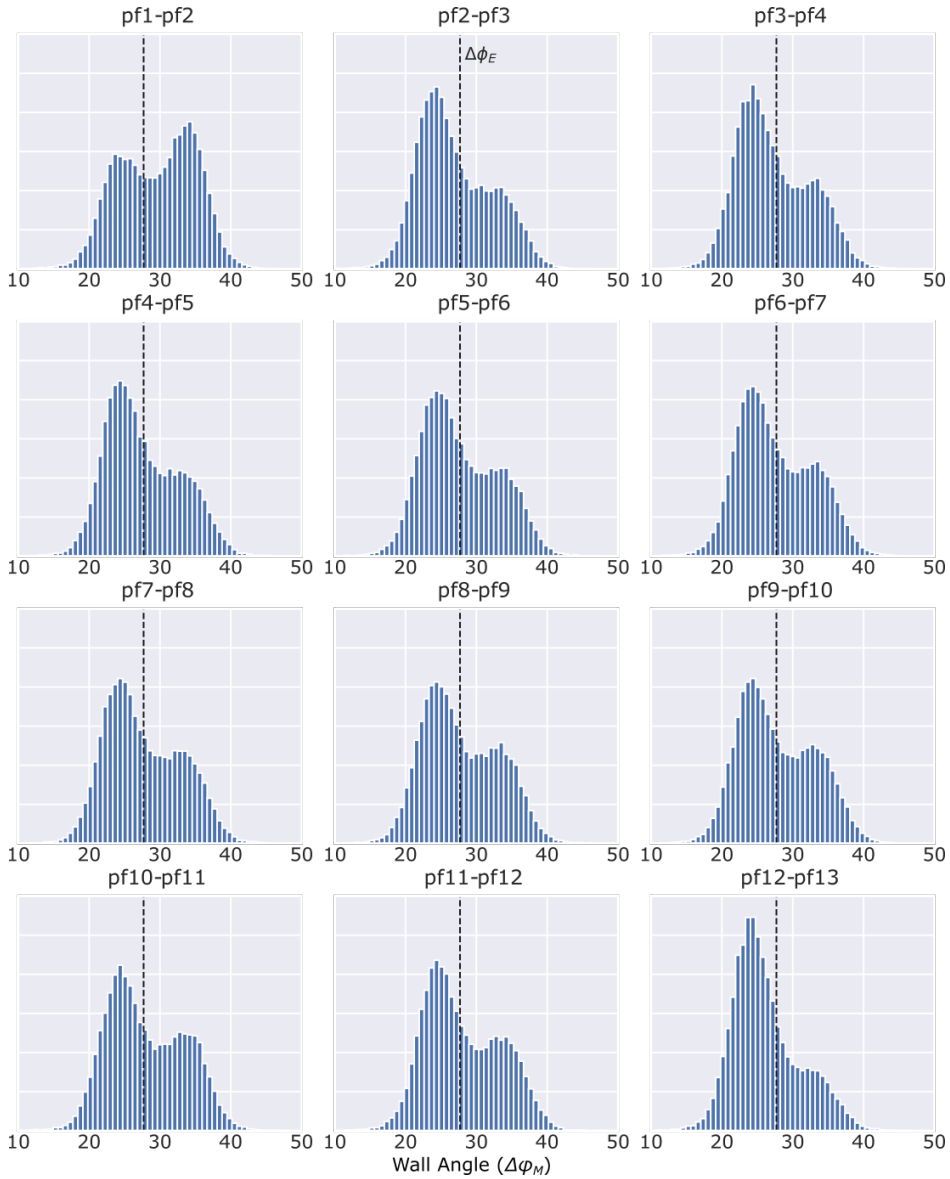

Figure S7. Wall angle distributions for individual protofilament pairs in the 13-protofilament Taxol microtubule symmetry type. The dashed line represents $\Delta\varphi_E$. While most of these distributions are essentially indistinguishable, the wall angle behavior diverges for the two protofilament pairs adjacent to the seam. To the left of the seam (pf1-pf2 top left), the high curvature state is more populated compared with the rest of the wall, while to the right of the seam (pf12-pf13, bottom right) the low curvature state is more populated. For discussion of this behavior, see Figure S8B.

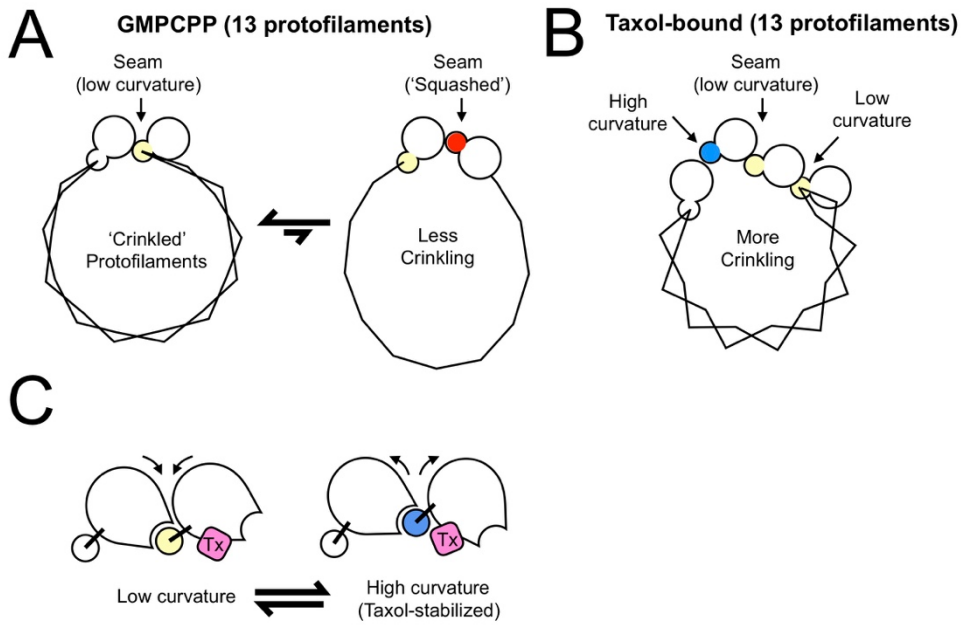

Figure S8. Effects of Taxol on microtubule wall dynamics. (*A*) Reference schematic depicting the observed structural states in 13-microtubules from the GMPCPP sample. (*B*) Schematic of the wall shape of a Taxol-bound microtubule. Compared with the GMPCPP-stabilized microtubule in *(A)*, several differences are evident. The 'squashed'-seam subpopulation disappears, presumably due to strain relaxation in the non-seam lateral contacts, whose average hinge angle (average of the two states in *(C)*) better matches the 13-protofilament microtubule geometry. Moreover, the wall angles in the Taxol-stabilized sample make larger fluctuations about the average hinge angle ($\Delta\varphi_E$) (i.e. are more 'crinkled') due to an increased tendency to form the high-curvature lateral contact *(C)*, together with subtle changes in the low- and high-curvature hinge angle distributions induced by Taxol (compare Figure 4C, E with Figure 5A, B). Notably, however, Taxol fails to have this effect at the seam *(B)*, where the hinge angle behavior is essentially indistinguishable from that of the GMPCPP sample (low curvature wall angle is strongly favored; Figure 4C, E, Figure 5A, B and Figure 6D, E). A characteristic, asymmetric deformation is observed amongst the four protofilaments closest the seam (Figure S6): the lateral contact to the left of the seam shows an increased preference for the high-curvature state, while the opposite is true for the lateral contact to the right of the seam. The precise origin of this asymmetric seam behavior in the Taxol sample is unclear, but may reflect a kind of 'phase boundary' between two lateral contact types with distinct properties (seam vs. non-seam)– reminiscent of asymmetric perturbations introduced within an actin filament upon the binding of a single cofilin molecule [16].

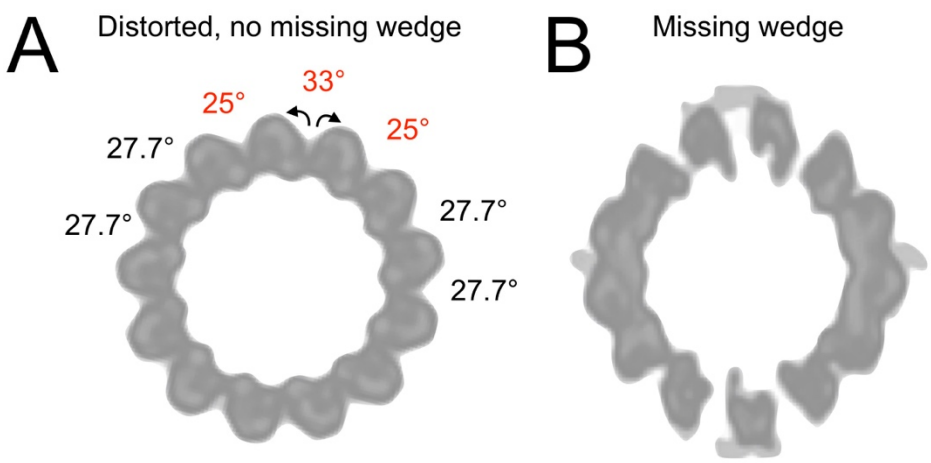

Figure S9. Simulating the effects of cryo-tomographic reconstruction on a distorted microtubule. (A) Data from the Taxol sample was used to selectively reconstruct a microtubule 3D map with a single, localized wall deformation similar to the 'high-angle' conformation depicted in Fig. 5 (corresponding to a 'wall angle' of ~33°, which is 5 degrees above the symmetric value (27.7°). A low-pass filter (20Å) was then applied to the volume, yielding a conservative estimate of the signal loss expected in a tomogram (where the resolution is still much better than can currently be realized experimentally). The localized distortion (protofilament rotations denoted with curved arrows) is quite subtle and not readily visible to the eye. (B) Upon simulating the missing wedge (applying a wedge mask to the volume Fourier transform), the resulting map artifacts (right-hand panel in the Figure below) overwhelm the differences that can be attributed to the original wall deformation. Fitting individual protofilament PDB models into the simulated tomogram confirms that large fitting errors would prevent identification of the distorted wall region, despite the idealized, noise-free tomographic imaging conditions that were simulated.

Table S1: Reported resolutions and helical parameters for all reconstructed volumes.

	Asymmetric Reconstruction		Asymmetric Helical Parameters		Symmetric Reconstruction		Protofilament Reconstruction	
	Number of particles	Resolution (Å)	Helical Rise	Helical Twist	Number of particles	Resolution (Å)	Number of particles	Resolution (Å)
GMPCPP 13-PF	8115	7.3	82.89	0.26	-	-	105313	3.9
GMPCPP 14-PF	29070	4.5	82.89	-0.3	406980	4.1	403424	3.6
Taxol 12-PF	53091	4.1	83.2	0.92	ND	ND	221448	3.2
Taxol 13-PF	114406	4	83.17	0.14	554424	3.3	852332	2.9
Taxol 14-Pf	20456	6.2	83.06	-0.37	-	-	85666	3.7
Taxol 13-PF Low curvature state	-	-	-	-	-	-	258448	3.2
Taxol 13-PF High curvature state	-	-	-	-	-	-	164553	3.3

SI References

1. Shang, Z.G., et al., *High-resolution structures of kinesin on microtubules provide a basis for nucleotide-gated force generation.* Elife, 2014. **3**.
2. Liu, D.F., et al., *Structural basis of cooperativity in kinesin revealed by 3D reconstruction of a two-head-bound state on microtubules.* Elife, 2017. **6**: p. 1-21.
3. Castoldi, M. and A.V. Popov, *Purification of brain tubulin through two cycles of polymerization-depolymerization in a high-molarity buffer.* Protein Expr Purif, 2003. **32**(1): p. 83-8.
4. Zheng, S.Q., et al., *MotionCor2: anisotropic correction of beam-induced motion for improved cryo-electron microscopy.* Nature Methods, 2017. **14**(4): p. 331-332.
5. Zhang, K., *Gctf: Real-time CTF determination and correction.* Journal of Structural Biology, 2016. **193**(1): p. 1-12.
6. Ludtke, S.J., P.R. Baldwin, and W. Chiu, *EMAN: Semiautomated software for high-resolution single-particle reconstructions.* Journal of Structural Biology, 1999. **128**(1): p. 82-97.
7. Sindelar, C.V. and K.H. Downing, *The beginning of kinesin's force-generating cycle visualized at 9-A resolution.* Journal of Cell Biology, 2007. **177**(3): p. 377-385.
8. Scheres, S.H.W., *RELION: Implementation of a Bayesian approach to cryo-EM structure determination.* Journal of Structural Biology, 2012. **180**(3): p. 519-530.
9. Zhang, R. and E. Nogales, *A new protocol to accurately determine microtubule lattice seam location.* Journal of Structural Biology, 2015. **192**(2): p. 245-254.
10. Heymann, J.B., *Single particle reconstruction and validation using Bsoft for the map challenge.* J Struct Biol, 2018. **204**(1): p. 90-95.
11. Pettersen, E.F., et al., *UCSF chimera - A visualization system for exploratory research and analysis.* Journal of Computational Chemistry, 2004. **25**(13): p. 1605-1612.
12. Chretien, D. and R.H. Wade, *New Data on the Microtubule Surface Lattice.* Biology of the Cell, 1991. **71**(1-2): p. 161-174.
13. Timoshenko, S., D.H. Young, and W. Weaver, *Vibration problems in engineering*. 1937, New York: Wiley.
14. Croll, T.I., *ISOLDE: a physically realistic environment for model building into low-resolution electron-density maps.* Acta Crystallogr D Struct Biol, 2018. **74**(Pt 6): p. 519-530.
15. Goddard, T.D., et al., *UCSF ChimeraX: Meeting modern challenges in visualization and analysis.* Protein Sci, 2018. **27**(1): p. 14-25.
16. Huehn, A.R., et al., *Structures of cofilin-induced structural changes reveal local and asymmetric perturbations of actin filaments.* Proc Natl Acad Sci U S A, 2020. **117**(3): p. 1478-1484.